Design and Manufacture of a Linear Actuator Based on Magnetic Screw Transmission

Ling, Zhijian; Zhao, Wenxiang; Rasmussen, Peter Omand; Ji, Jinghua; Jiang, Yang; Liu, Zhengmeng

Published in:
IEEE Transactions on Industrial Electronics

DOI (link to publication from Publisher):
10.1109/TIE.2020.2967731

Publication date:
2021

Document Version
Accepted author manuscript, peer reviewed version

Design and Manufacture of a Linear Actuator Based on Magnetic Screw Transmission

Zhijian Ling, *Student Member IEEE*, Wenxiang Zhao, *Senior Member IEEE,*
Peter Omand Rasmussen, *Member IEEE,* Jinghua Ji, Yang Jiang, Zhengmeng Liu

***Abstract*—This paper proposes a practical design guide for a linear electromagnetic actuator based on the concept of magnetic screw transmission, in which manufacture and assembly technologies are investigated. The surface-inserted design is firstly used to form a required helical-shape magnetic pole, which exhibits simple processing, high precision, and robust structure. Moreover, the three-dimensional finite element analysis (FEA) aided design different topologies are developed, with the goal of optimizing thrust force. Besides, the different number of permanent-magnet (PM) segmentation is firstly proposed to reduce the cogging effect. Afterward, the linear actuator integrates rotary machine and magnetic screw overall together to construct a compact design and decouples the magnetic circuits. The decoupling design focuses on the self-shielding effect of the Halbach PM array, and the special bearing supports are selected to avoid the eccentricity. Finally, a prototype is built using the developed techniques. Experiments are carried out on a linear test bench, verifying the theoretical analysis.**

***Index Terms*—Linear electromagnetic actuator, magnetic transmission, manufacture and assembly, finite element analysis, permanent-magnet.**

NOMENCLATURE

ξ	Cutting angle of discrete PM (deg).
α	Angle of discrete PM (deg).
τ_p	Pole-pitch of magnetic screw (mm).
w_p	Width of discrete PM (mm).
h_p	Thickness of discrete PM (mm).
z_d	Relative linear position (mm).
θ_r	Relative angle position (deg).
λ	Magnetic lead (mm).
ω_r	Rotor angle speed (rad/s).
v_t	Translator linear speed (m/s).
F_t	Thrust force (kN).
T_n	Rotor torque (N.m).
G	Equivalent magnetic gear ratio.
P_r, P_t	Power of rotor, translator.
$S_{surface}$	Operating surface area (mm^2).
$F_{surface}$	Force per area (MN/m^2).
L_s, L_r, L_t	Length of stator, rotor, translator (mm).
β	Angle of back-iron bulge (deg).
k_c	Magnetic coverage.
h_b	Height of bulge (mm).
n_t, n_r	Number of segmentation.
$G_{com\text{-}1}$, $G_{com\text{-}2}$	Equivalent magnetic permeability.
k_d, k_p, k_w	Distribution, pole-pitch, winding factor.
q, δ, τ	Slots phase, angular pitch, pole distance.
S, Z, N	Number of slots, poles, phase.
B_{rem}	Magnet remanent (T).
H_C	Magnet coercivity (kA/m).
J	Current density (A/mm^2).
i_a, i_b, i_c	Current of phases (A).

Manuscript received January 15, 2019; revised June 12, 2019, August 26, 2019, October 23; accepted December 23, 2019. This work was supported in part by the National Natural Science Foundation of China (Projects 51977099 and 51777090), in part by the Key Research and Development Program of Jiangsu Province (BE2018107), in part by the Six Talent Peaks Project of Jiangsu Province (2017-KTHY-011), and in part by the Priority Academic Program Development of Jiangsu Higher Education Institutions. (*Corresponding author: Wenxiang Zhao*)

Z. Ling, W. Zhao, J. Ji, and J. Yang are with the School of Electrical and information Engineering, and also with the Jiangsu Key Laboratory of Drive and Intelligent Control for Electric Vehicle, Jiangsu University, Zhenjiang 212013, China (e-mail: lingzhijian0826@163.com; zwx@ujs.edu.cn; jjh@ujs.edu.cn; 1547728149@qq.com).

P. O. Rasmussen is with the Department of Energy Technology, Aalborg University, DK-9220 Aalborg, Denmark (e-mail: por@et.aau.dk).

Z. Liu is with the Department of Electronic and Electrical Engineering, University of Sheffield, Sheffield S1 3JD, U.K. (e-mail: zliu58@sheffield.ac.uk)

I. INTRODUCTION

TO satisfy linear motion applications, various types of linear actuators have been investigated, leading to an increased interest toward linear direct-drive actuators [1]-[3]. Conventional linear motion technologies are realized by using roller/ball screws, with contact transmission. The roller/ball screw linear actuator converting rotary-linear motion and exhibits a significantly high force density. However, mechanical wear, loss, gear noise, and regular lubrication are inevitable. Thus, the mechanical contact transmission may reduce reliability and increase the maintenance requirement [4]. Linear permanent-magnet (PM) machines offer many advantages, in terms of high dynamic and high precision, but its thrust force density is relatively poor [5]. Some novel linear machine topologies have been proposed to further improve the thrust force density, such as flux-modulation structure and tubular PM machine. Nevertheless, the improvement of thrust force density is limited, and also increases the complexity of manufacturing [6]-[8].

Recently, the concept of non-contact magnetic gear coupling transmission has received increased attention [9]-[11]. Similar to the mechanical gears, the magnetic gear can transform torque or thrust force by the magnetic field. Hence, it offers some distinct advantages, namely, free maintenance, improved reliability, overload protection, and physical isolation between input and output. By extending this idea to the linear structure and adopting a helical magnetic field, the concept of the magnetic screw transmission was proposed. The magnetic screw offers high thrust force density and high reliability [12], [13]. Due to the advantages of magnetic screw transmission actuators, various design and modeling procedures for magnetic transmissions were reported [14]-[18].

However, the main drawback of the existing magnetic screws is the manufacturing process of the high-performance helical PM poles. The techniques of structure simplification and manufacturing processes are essential in promoting development. In [19], [20], the reluctance magnetic screws were proposed, offering fewer magnet and simpler manufacture structures. However, the reluctance structure will reduce the thrust force performance significantly.

In [21], a non-ideal helix magnetic screw with discrete PM blocks was proposed, indicating that the more discrete PM blocks used, the closer the approximation of an ideal helical magnetic field will be attained. If a low number of the discrete PM blocks are used to form the helical magnetic poles, the thrust force tends to become much lower and more distorted. Consequently, the fabrication process and assembly of the high-performance magnetic screw will be time consuming and expensive. Refs. [22] and [23] investigated several PM configurations to realize the magnetic screw, and a manufacturing approach is proposed for forming a helical magnetic pole approximately. However, the assembly precision and mechanical strength are relatively low. Moreover, the PM radial magnetization process is difficult.

In addition to manufacturing, the integrated design of the magnetic screw and rotary machine have also received widespread attention. In [24], Vitale proposed a rotary-linear actuator, based on the rotary machine surrounding the magnetic screw. This linear actuator is well suited for high-force, high-reliability and short-stroke applications such as ventricle assist device and aerospace actuation. Then, this concept was redesigned in [25], and compared with the existing linear tubular PM machine, verifying the advantages of the magnetic screw linear actuator in terms of force, weight, and material cost. However, the assembly technologies and magnetic decoupling of the integrated design have not been investigated.

In [26], Pakdelian *et al*. proposed an electric machine integrated with a magnetic screw, which mechanically connects the magnetic screw rotor to the rotary machine. This topology enables the rotary machine and magnetic screw to operate independently, but the connecting devices and the linear bearings are external, resulting in a relatively large size. Moreover, since the linear bearings are mounted on one side of the translator, the non-uniformly stress points will cause an even eccentricity. The eccentricity deflection will result in physical contact between the rotor and the translator [13].

Refs. [27] and [28] presented several magnetic screw integrated design for wave energy conversion and suspension systems. The main functions of those prototypes are to convert linear-to-rotary motion and achieve energy recovery. In those topologies, the standard linear guide similar to the dry sliding bearing is employed, which is mounted on the outside of the translator. The surface of the translator is in direct contact with the dry sliding bearing, which will cause the discrete PM to fall off and the friction force is large. Also, the magnetic circuits of the rotary part and the magnetic screw is not investigated.

The purpose of this paper is to investigate the key issues in fabrication, assembly, and test of a linear electromagnetic actuator based on the magnetic screw. The surface-inserted topology is firstly employed for forming the required helical magnetic poles. Besides, several new technologies are presented to improve the performance of force and cogging effect, such as the different number of segmentation, radial magnetization. Furthermore, the systematic design integrates the PM rotary machine and the magnetic screw, in which the magnetic circuits are decoupled. The special bearing supports are selected to avoid eccentricity. The rest of this paper is organized as follows. In Section II, the configuration and operation principle of the linear actuator is described. Section III investigates the optimize and manufacture of the magnetic screw. After this, the integrated assembly of the magnetic screw and rotary machine are presented in Section IV. In Section V, a prototype is built, and the experimental results are presented. Finally, the conclusion is drawn in Section VI.

II. Topology and Operation Principle

A. Topology

Fig. 1 shows the basic structure of the proposed linear electromagnetic actuator. It can be seen that this design consists of three parts, namely, a stator with fractional-slot concentrated-windings (FSCW), a common rotor rotating about the *z*-axis, and an inner translator moving back and forth along the *z*-axis. Since the rotor and magnetic screw nut share the same rotor core, it is necessary to study the magnetic coupling between the PM machine and the magnetic screw. Therefore, the machine rotor uses Halbach magnetized PM array, which is benefits for the effect of magnetic self-shielding.

When the rotary machine and magnetic screw are integrated overall together, the manufacture and assembly technology must be taken into account. Based on the material properties of high-performance sintered rare earth PM, such as NdFeB, it is very difficult to manufacture an ideal helical magnetic pole. Fig. 2 shows the new surface-inserted design with discrete PMs and back-iron bulges to simplify the assembly process while forming the required helical magnetic pole and a robust structure. The cutting angle ξ for the two sides of discrete PM with respect to the top edge is given by

$$\xi = \arctan\left[\frac{w_p \alpha}{2\pi r \sin(\alpha/2)}\right] \tag{1}$$

where r is the inner radius of the discrete PM block, α is the angle of the discrete PM block and τ_p is the pole-pitch of PM.

This article has been accepted for publication in a future issue of this journal, but has not been fully edited. Content may change prior to final publication. Citation information: DOI 10.1109/TIE.2020.2967731, IEEE Transactions on Industrial Electronics

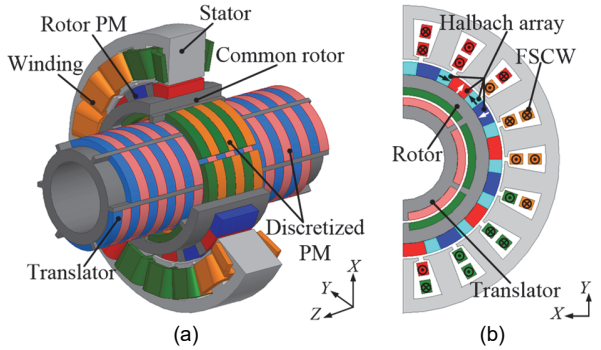

Fig. 1. View of proposed linear electromagnetic actuator. (a) 3-D view. (b) 2-D front view.

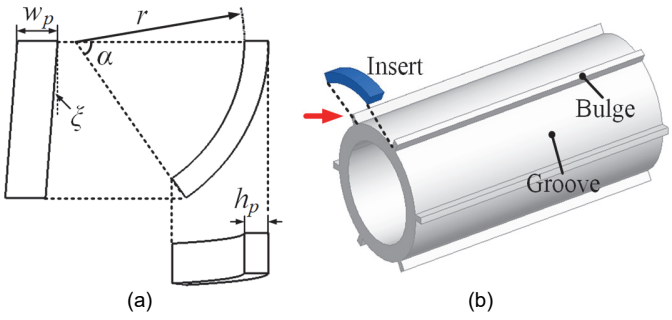

Fig. 2. Structure of proposed surface-inserted method. (a) Discrete PMs. (b) Schematic of discretized PM assembly.

B. Operation Principle of Magnetic Screw

Based on the helical magnetic field, the magnetic screw transmission is capable of converting rotational motion into linear motion and vice versa. The relationship between the relative position and magnetic field distribution of the magnetic screw is shown in Fig. 3. As the relative position z_d and θ_r between the magnetic poles increases, the magnetic field distributions along the axial direction becomes significant, resulting in the development of thrust force and torque. Therefore, there is an equivalent magnetic gear ratio G. By considering the power balance between the translator power P_t and rotor power P_r, the gear ratio of linear velocity v_t and rotary speed ω_r would be equal to the ratio of rotor torque T_n and translator thrust force F_t. In a 2-pole magnetic screw, as one complete circle (2π) rotation, the translator moves one lead λ. The equivalent magnetic gear ratio G can be expressed as

$$G = \frac{\omega_r}{v_t} = \frac{F_t}{T_n} = \frac{2\pi}{\lambda} \tag{2}$$

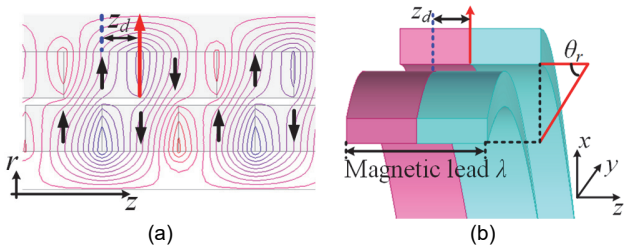

Fig. 3. Relative position between the translator and rotor. (a) 2-D equivalent model. (b) 3-D schematic.

III. Design and Manufacture of Magnetic Screw

A. Maximum Force Density Considerations

For the magnetic screw part, the air-gap length g, operating surface area $S_{surface}$, magnetic lead λ, and PM material properties will significantly affect the performance. The geometric parameter and the operating surface area of the magnetic screw are illustrated in Fig. 4. It can be seen that the operating surface area $S_{surface}$ is proportional to the active length L_r and operating radius R_{to}+g/2. Consequently, the operating surface area can be calculated by

$$S_{surface} = 2\pi(R_{to} + g/2)L_r \tag{3}$$

In magnetic transmission, the smaller the air-gap length g, the better the thrust force and flux density performance can be achieved [21]. The length of the air-gap g depends on the manufacturing precision, thus emphasizing the importance of the fabrication. Based on the proposed surface-inserted assembly method, the length of air-gap g is selected to be 1mm. Then, the thrust force per surface area $F_{surface}$ should be used to evaluate the thrust force capability can be expressed as

$$F_{surface} = \frac{F_t}{S_{surface}} = \frac{F_t}{2\pi(R_{to} + g/2)L_r} \tag{4}$$

For the fixed air-gap length g and PM thickness h_p, the ratio between the thrust force and the surface operating area $S_{surface}$ of the shear stress $F_{surface}$ is illustrated in Fig 5, which is as a function of the operating radius R_{to}+g/2 for different magnetic leads (twice of PM width w_p). It is observed that for a fixed magnetic lead λ, the thrust force per surface area $F_{surface}$ is approximately constant with the variations of the operating radius R_{to}+g/2. The variation of the $F_{surface}$ with different magnetic leads can be attributed to the flux leakage between the adjacent magnetic poles. Therefore, by considering the geometric constraints imposed by the rotary machine, and determining the appropriate operating radius R_{to}+g/2, magnetic thickness h_p, magnetic lead λ, and active length L_t.

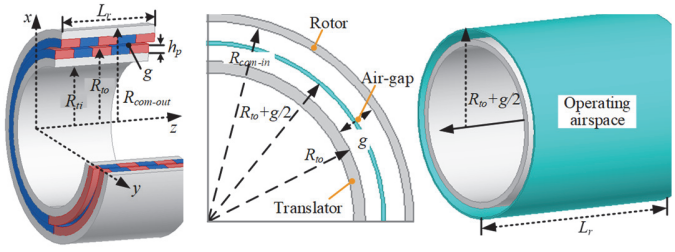

Fig. 4. Characteristic of magnetic screw. (a) Geometric parameter. (b) Operating surface area.

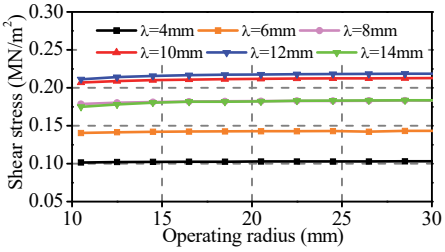

Fig. 5. Influence of shear stress as a function of operating radius and different lead with constant g and h_p (g=1mm, h_p=3mm).

This article has been accepted for publication in a future issue of this journal, but has not been fully edited. Content may change prior to final publication. Citation information: DOI 10.1109/TIE.2020.2967731, IEEE Transactions on Industrial Electronics

B. Manufacturing of Helical Magnetic Poles

The main difficulty of the magnetic screw lies in the fabrication of its helical magnetic pole. Thus, the surface-inserted structure is proposed with the discrete PMs and back-iron bulges, while forming a helical magnetic pole with high accuracy and robust structure. Fig. 6 shows several different topologies, including ideal discrete PM, PM-bugle, back-iron dovetail-bugle, half-bulge, and full-bulge.

Intuitively, the ideal discrete PM in Fig. 6(a) is much more realizable to process and less costly. However, during assembly, the positioning of these discrete PMs is quite difficult. Especially in a long translator, it suffers from the surface flatness, which directly affects the uniformity of the air-gap. The actual prototype is shown in Fig. 7(a). Therefore, it is necessary to employ some positioning auxiliary topologies to improve assembly accuracy. The magnetic screw prototype employing discrete PM with dovetail-bulge is shown in Fig. 7(b), by which the surface precision and flatness can be improved. However, the sintered NdFeB PM material suffers from poor processability, so the PM with dovetail-bulge is extremely difficult to manufacture, resulting in high processing costs. Also, the thickness of discrete PM is variable, which will affect the force performance and air-gap magnetic field density.

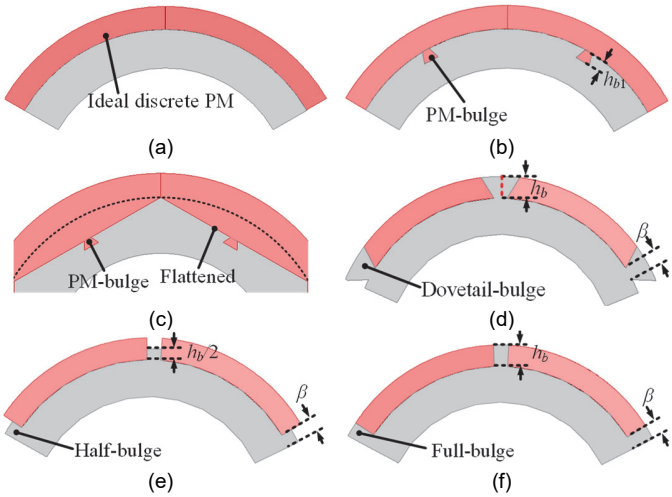

Fig. 6. Different topologies. (a) Ideal discrete PM. (b) PM-bulge. (c) Flattened PM-bulge. (d) Dovetail-bulge. (e) Half-bulge. (f) Full-bulge

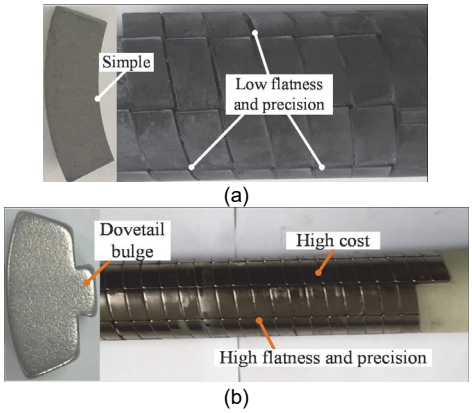

Fig. 7. Discrete PMs assembled. (a) Ideal discrete PM. (b) Dovetail-bulge PM.

The thrust forces of the different topologies are predicted by 3-D FEA, as illustrated in Fig. 8(a). The ideal discrete PM and PM-bulge topologies have slightly high values due to the high magnetic coverage. For the proposed surface-inserted structures, it can be seen that the shape of the bulges will affect the force performances. Especially in the dovetail-bugle structure, due to the variation of the magnetic permeability, the thrust force tends to become irregular and the amplitude decreased significantly. Then, in the half-bulge and full bulge topologies, it can be observed that the waveforms are relatively smooth and the amplitudes are similarly. For a clear description, their amplitude analysis is shown in Fig. 8(b). Considering force performance and manufacture, the full-bulge topology is selected and fabricated.

Fig. 8(c) shows the variation of the value of the thrust force with the angle of back-iron bulge β. By increasing the angle β, the thrust force value will be decreased due to the effect of the percentage of magnetic coverage k_c. Based on the processing level and material properties, the angle of discrete PM α is selected to be 55 degrees and the angle of bulge β is 5 degrees. The parameters of the surface-inserted magnetic screw are listed in Table I.

TABLE I
DESIGN SPECIFICATIONS OF MAGNETIC SCREW

Item	Value
Outer radius of rotor, $R_{com\text{-}out}$ (mm)	33
Thickness of common core (mm)	4.5
Outer radius of translator, R_{to} (mm)	24
Inner radius of translator, R_{ti} (mm)	16
Magnetic lead, λ (mm)	10
PM width, w_p (mm)	5
Active length, L_r (mm)	80
Translator length, L_t (mm)	204
Height of bulge, h_b (mm)	3
Magnetic screw air-gap, g_1 (mm)	1
Sleeve thickness, (mm)	0.3
PM thickness, h_p (mm)	3
Back-iron thickness, h_t (mm)	5
Angle of discrete of PM, α (deg)	55
Angle of bulge, β (deg)	5
Magnetic coverage, k_c (%)	91.6

The proposed surface-inserted assembly process is shown in Fig. 9. The back-iron is designed as bulges and grooves for ease of the discrete PMs assembly, and achieve circumferential positioning. Before assembling the PMs, the axial restrictors are mounted at the end of the back-iron, forming a preliminary helical positioning. Then, the discrete PMs can be easily pushed into the grooves from the other end of the bulges, resulting in a high accuracy and robustness topology. Fig. 10 shows the prototype of the surface-inserted magnetic screw. The aluminum axial restrictors are installed on the end of the back-iron and achieve an axial helical positioning. The magnetic field density of the surface-inserted magnetic screw is measured by a Gauss meter to verify the surface remanence of the sintered NdFeB PM. After the assembly of discrete PMs, a stainless steel sleeve with 0.3mm thickness is machined and placed on the translator to fix the radial direction of the discrete PMs. Then, the epoxy resin is poured into the gap between the stainless steel sleeve and back-iron for packaging.

This article has been accepted for publication in a future issue of this journal, but has not been fully edited. Content may change prior to final publication. Citation information: DOI 10.1109/TIE.2020.2967731, IEEE Transactions on Industrial Electronics

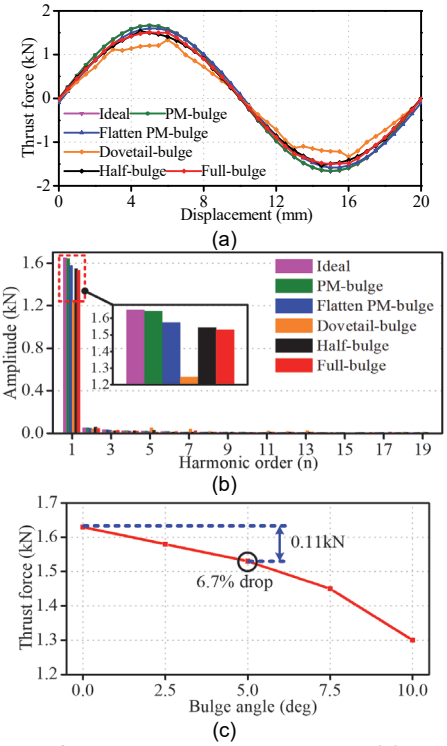

Fig. 8. Thrust force comparison by 3-D FEA. (a) Waveform. (b) Amplitude analysis. (c) Variation of bulge angle β.

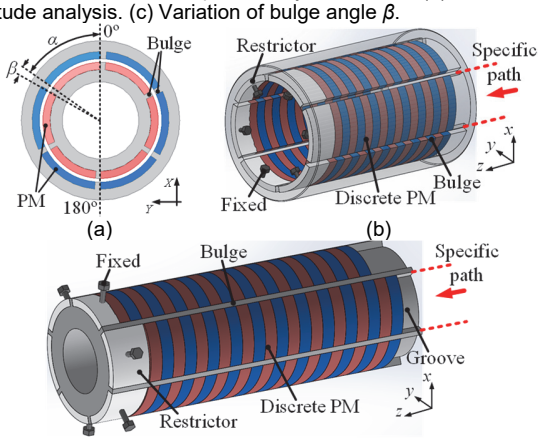

Fig. 9. Method to form the helical magnetic poles. (a) 2-D front view. (b) Rotor. (c) Translator.

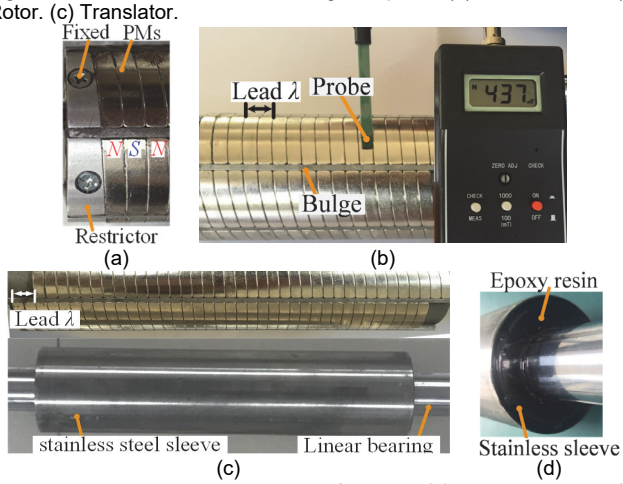

Fig. 10. Helical magnetic pole manufactured. (a) Axial restrictors. (b) Remanence test. (c) Stainless steel sleeve. (d) Epoxy resin.

C. Novel Method to Reduce Cogging

Since the magnetic screw is made of discrete PMs and surface-inserted in the bulges to form a helical magnetic pole, the effect of the cogging must be taken into account. The 3-D FEA model of the surface-inserted magnetic screw with the different number of segmentation is developed, as shown in Fig. 11. For a fair verification, the same percentage of magnetic coverage k_c is employed. The angle of the bulge variations with the number of segmentation and the relationship is given by

$$n_t \times \beta_t = n_r \times \beta_r \tag{5-a}$$

$$\alpha_r = 2\pi / n_r - \beta_r \tag{5-b}$$

$$\alpha_t = 2\pi / n_t - \beta_t \tag{5-c}$$

where n_t and n_r are the different number of segmentation on translator and rotor, β_t and β_r are the angles of the bulge, α_t and α_r are the angle of discrete PM, respectively.

The force and torque performances of the different number of segmentation magnetic screws are shown in Fig. 12. It can be seen that the variation of the number of segmentation has little influence on the thrust force waveform and amplitude, but the ripple of the torque changes significantly. This is because, in a surface-inserted magnetic screw, the torque ripple frequency and amplitude, similar to a rotary switched reluctance motor, depend on the bulges position between the translator and rotor.

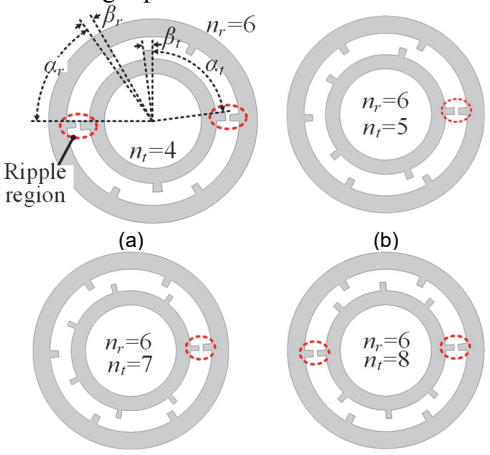

Fig. 11. Magnetic screw with a different number of segments. (a) 6-4. (b) 6-5. (c) 6-7. (d) 6-8.

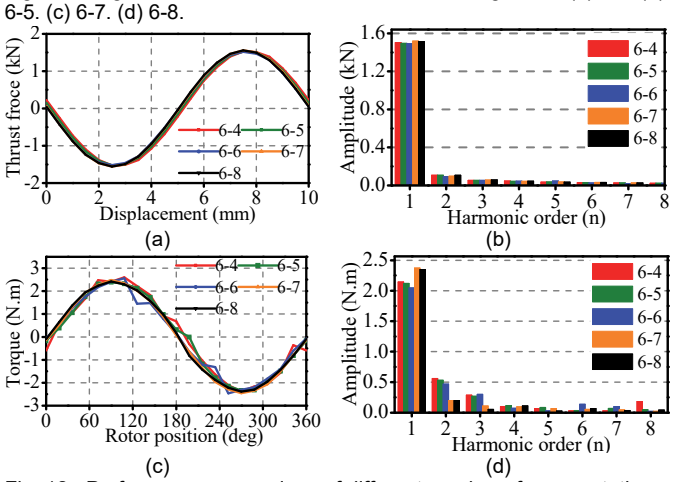

Fig. 12. Performance comparison of different number of segmentation. (a) Force. (b) Force amplitude. (c) Torque. (d) Torque amplitude.

This article has been accepted for publication in a future issue of this journal, but has not been fully edited. Content may change prior to final publication. Citation information: DOI 10.1109/TIE.2020.2967731, IEEE Transactions on Industrial Electronics

Also, the analysis of the cogging effects caused by the simultaneous movement of the rotor and translator is very important. It will directly reflect the performance of the linear actuators, such as ripple and dynamic. Fig. 13 shows a simplified method to evaluate the cogging effect under no-load and full-load. It can be seen that as the initial relative angle θ_r changes, the initial relative displacement z_d changes, accordingly. Under the no-load condition, the relative position between the translator and the rotor is aligned (z_d=0). Then, as the same principle, when the initial relative displacement z_d between the translator and the rotor is a quarter of magnetic lead (z_d=λ/4), the full-load cogging effect is investigated.

The force ripple and torque ripple of the n_r=6, n_t=6 structure, and n_r=6, n_t=7 structure are shown in Fig. 14. The period of the cogging effect is one arc angle of the discrete magnet and bulge. In the full-load operation, it is evident that the ripple of force and torque have been effectively suppressed using the different number of segmentation, decreasing from 7.43% to 2.97%, and 15.9% to 7.5%, respectively. Therefore, selecting a different number of segments on the translator and the rotor can effectively reduce the cogging effect, such as 6 segments on the rotor and 7 segments on the translator.

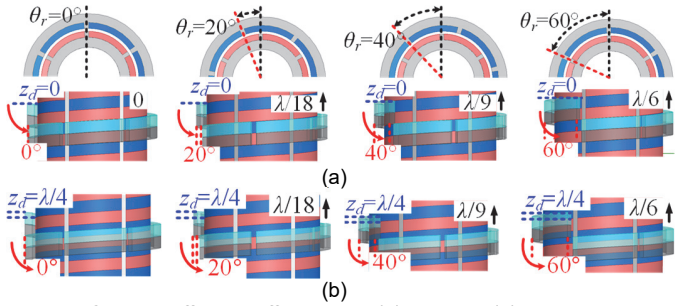

Fig. 13. Cogging effect at different load (a) No-load. (b) Full-load.

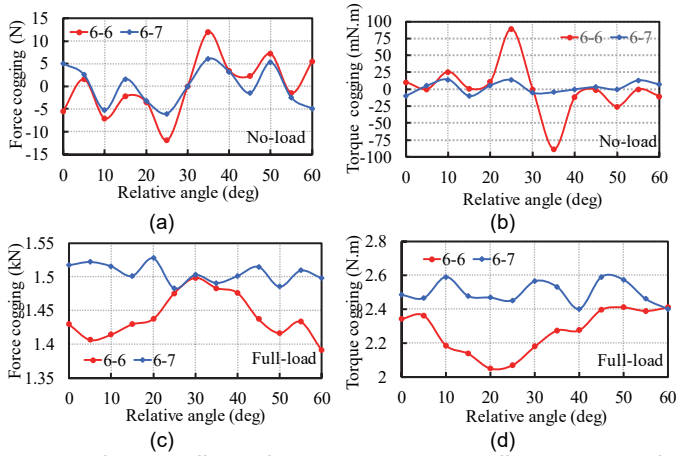

Fig. 14. Cogging effects of magnetic screw with different number of segmentation. (a) No-load force cogging. (b) No-load torque cogging. (c) Full-load force cogging. (d) Full-load torque cogging.

D. Radial Magnetization of Discrete PM

For the fabrication of surface-inserted helical magnetic poles, there are two main types of magnetization for discrete PMs, such as radial and parallel, as shown in Figs. 15(a) and (b). In practice, the parallel magnetization is much easier to achieve than radial magnetization. However, it is worth noting that the magnetization direction has a significant effect on the air-gap helical magnetic field distribution. In order to achieve radial magnetization of the discrete PM, a simple magnetization fixture is designed, which is made of a high permeability material such as CoFe, as shown in Fig. 15(c).

Fig. 16 shows the radial magnetic field components of the segmented helical magnetic pole with radial and parallel magnetization PM, respectively. In the radial magnetization structure, the magnetic field component is relatively smooth, and its slight fluctuation is mainly caused by the segmentation. However, the parallel magnetization leads to a distorted magnetic field distribution. This is because the parallel magnetization has not only a radial component but also existence an axial component. Taking the surface-inserted magnetic screw with 6 segments rotor and 7 segments translator as an example, the distortion of magnetic distribution will be directly reflected in the torque performances.

Apart from the amplitude and ripple, the magnetic losses are also investigated. It mainly consists of eddy-current loss and iron loss. In the radial magnetization, there are almost no extra harmonics except for the operating harmonic. Fig. 17 shows the helical magnetic field MMF analysis and magnetic losses of each part of the magnetic screw with the translator speed at 0.3 m/s. It can be seen that at low-speed operation, the magnetic losses are almost negligible. Therefore, in this design, the radial magnetization discrete PM is employed.

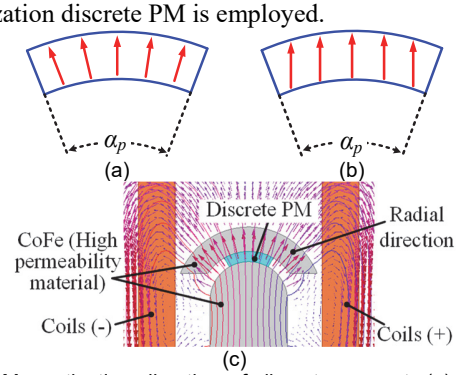

Fig. 15. Magnetization direction of discrete magnet. (a) Radial. (b) Parallel. (c) Radial magnetization schematic.

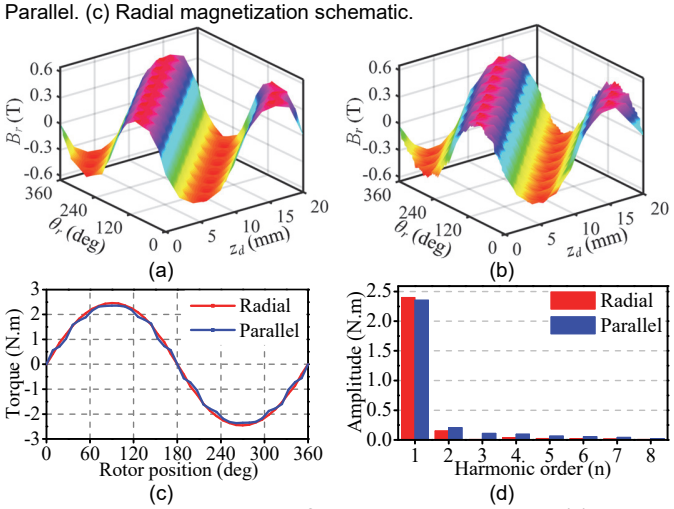

Fig. 16. Radial air-gap magnetic field distribution and torque. (a) Radial. (b) Parallel. (c) Torque. (d) Torque amplitude.

This article has been accepted for publication in a future issue of this journal, but has not been fully edited. Content may change prior to final publication. Citation information: DOI 10.1109/TIE.2020.2967731, IEEE Transactions on Industrial Electronics

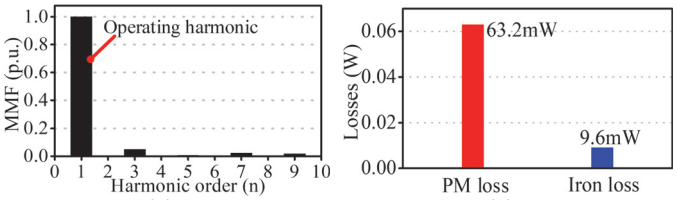

Fig. 17. Helical magnetic field MMF and losses. (a) MMF harmonic. (b) Magnetic losses.

IV. Integration Design and Assembly

This linear electromagnetic actuator is to integrate a rotary PM machine and a magnetic screw overall together, in which they impose any geometric constraint on each other. Thus, the optimization design of the linear electromagnetic actuator entails simultaneous consideration of magnetic decoupling and electromagnetic performances both the magnetic screw and the rotary machine.

A. Magnetic Decoupling Analysis

The magnetic circuits decoupling is a critical step in integrated design. Several different kinds of decoupling structures are original proposed and evaluated, as shown in Fig. 18, namely, Radial-surface, Radial-embedded, Halbach-surface, and Halbach-embedded. In the radial array structure, it can be seen that the radial magnetic flux path depends on the silicon steel yoke. Thus, there are two layers of the magnetic yoke, one for the PM machine and the other for the magnetic screw. This will result in a large volume of the common region and increase manufacture difficulty.

Then, in the embedded magnetic screw structure, the role of the internal magnetic yoke can be almost ignored. However, the embedded helical magnetic poles suffer from difficulty manufacture and assemble. Therefore, based on the decoupling effect and manufacturing considerations, the Halbach-surface structure is selected and manufactured.

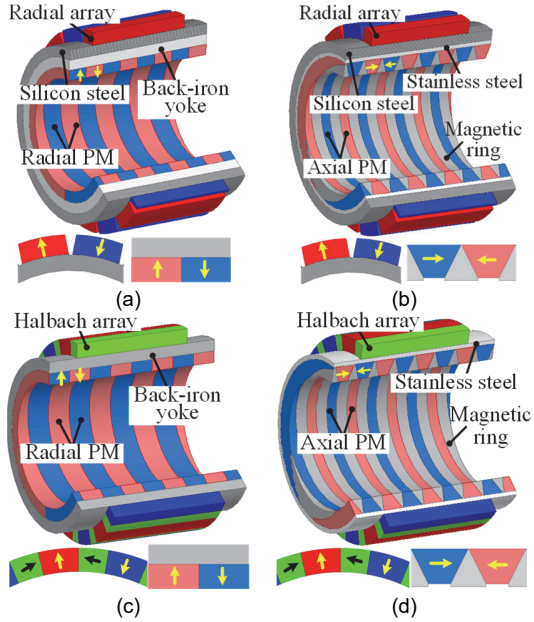

Fig. 18. Different kinds of decoupling models. (a) Radial-surfaced. (b) Radial-embedded. (c) Halbach-surfaced. (d) Halbach-embedded.

Fig. 19 shows the magnetic flux paths and geometric parameters of the Halbach-surfaced structure. The magnetic flux paths are in the circumferential direction and the axial direction, respectively. Based on the analysis of the magnetic flux path, the equivalent magnetic circuit model of the PM machine and the magnetic screw is established, respectively, as shown in Fig. 20. Thus, the equivalent magnetic permeability in the common back-iron core is divided into a circumferential $G_{com\text{-}1}$ and an axial $G_{com\text{-}2}$ can be expressed as

$$G_{com-1} = \mu_r \mu_0 \frac{L_s (R_{com\text{-}out} - R_{com\text{-}in})}{\pi R_{ro} (\alpha_1 + \alpha_2)/180^\circ} \tag{6-a}$$

$$G_{com-2} = \mu_r \mu_0 \frac{\pi (R_{com\_out}^2 - R_{com\_in}^2)}{w_{pm}} \tag{6-b}$$

where μ_r and μ_0 are the relative permeability of nonlinear magnetic material and the vacuum permeability, respectively. L_s, R_{ro}, $R_{com\text{-}out}$, $R_{com\text{-}in}$, and w_{pm} are the length, radius, and width of the geometry, respectively. α_1 and α_2 are the angle of radially and axially magnetized PM, respectively.

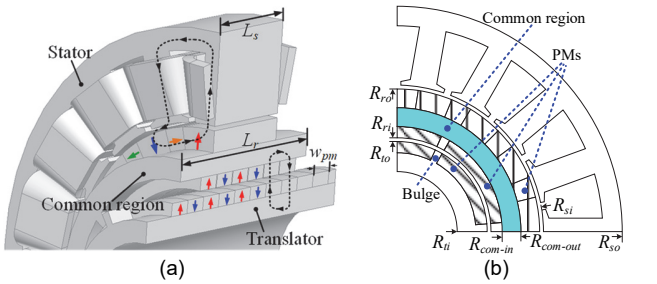

Fig. 19. Magnetic circuit and geometric parameter. (a) Flux path. (b) Geometric parameter.

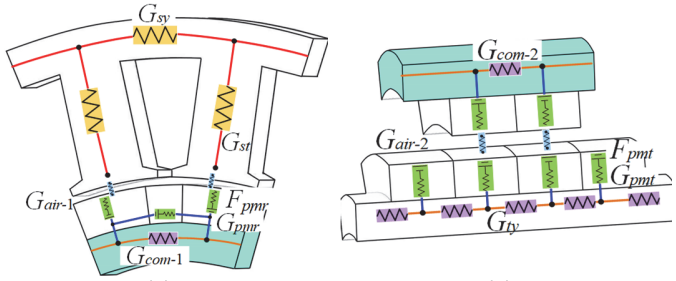

Fig. 20. Equivalent magnetic circuit model. (a) PM machine. (b) Magnetic screw.

The PM machine rotor employs a Halbach magnetized PM array, and the effect of self-shielding is an important technique to realize magnetic decoupling. First, based on the inner diameter of the PM machine, the number of rotor PM poles is determined. The more PM poles used, the better the self-shielding effect will be attained. According to the size and manufacture, 16 poles Halbach array is selected, as shown in Fig. 21. Also, the external and internal magnetic field distributions and magnetic field densities of the 16 poles Halbach array are presented. It can be easily observed that the external field exhibits much higher magnetic fluxes than the internal field, and the peak value of the internal magnetic field density is only 0.07T, while that of the external one is 0.63T.

This article has been accepted for publication in a future issue of this journal, but has not been fully edited. Content may change prior to final publication. Citation information: DOI 10.1109/TIE.2020.2967731, IEEE Transactions on Industrial Electronics

To further validate this point, the 3-D FE model is built. In order to accurately exhibit the analysis results, a high-density mesh is set, as shown in Fig. 22(a). Fig. 22(b) shows the 3-D magnetic field distribution. For a clear exhibit the independence of the magnetic field, the minimum scale of the magnetic density is set to be 0.2T. It is evident that in the common back-iron core there is almost only an axial magnetic field generated by the magnetic screw PMs.

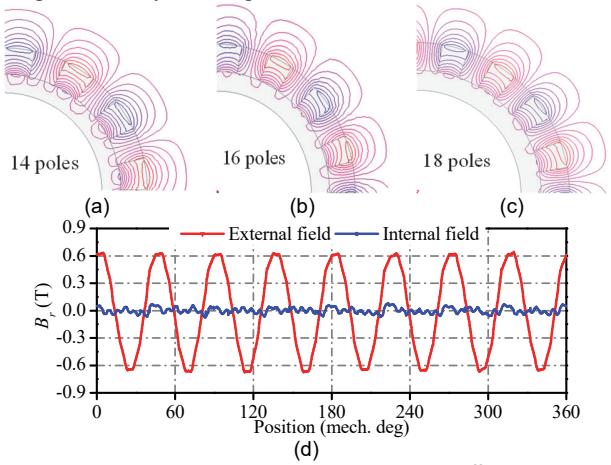

Fig. 21. Halbach array magnetic distribution with different number of poles. (a) 14 poles. (b) 16 poles. (c) 18 poles. (d) External and internal flux density.

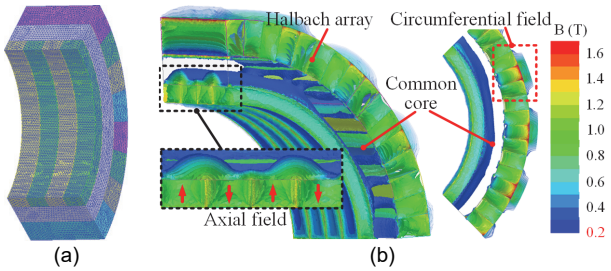

Fig. 22. 3-D FE model. (a) Meshes. (b) Magnetic field distribution.

B. Design of Rotary Machine

The choice for rotary machine types depends on the electromagnetic performance, application background, and optimization objectives. In this linear electromagnetic actuator, an FSCW-PM machine is selected for the rotary part. Also, it should be noted that in other designs, synchronous reluctance motors or induction motors may be superior to the FSCW-PM machine. Then, based on the number of rotor PM poles, in order to obtain a high winding coefficient, the number of stator slots is selected to be 18. In this 3-phase FSCW-PM machine with 18-slots and 16-poles, the winding factor k_w is 0.945, which is the inherent advantage of FSCW structure. The principle of slot number selection can be expressed as

$$k_d = \frac{sin(q\delta/2)}{q \cdot sin(\delta/2)} = 0.96\,,\quad k_p = \sin(\frac{1}{\tau}\cdot\frac{\pi}{2}) = 0.985$$
$$k_w = k_d \cdot k_p = 0.945 \tag{7}$$

where q is the number of slots per pole per phase, δ is the angular slot pitch, and τ is the pole distance.

The assembly process of the Halbach array is shown in Fig. 23. It can be seen that the aluminum tooling components are in turn replaced by different magnetized PMs and bonded to the back-iron core. After the Halbach array PMs are fixed, it is encapsulated with an epoxy resin to enhance the mechanical strength. Based on the advantages of the high slot fill concentrated winding, the slot fill rate of this prototype is 60.5%. The winding arrangement is shown in Fig. 24(a). Fig. 24(b) illustrates the prototype of stator and winding. The windings arrangements are presented in Fig. 24(c).

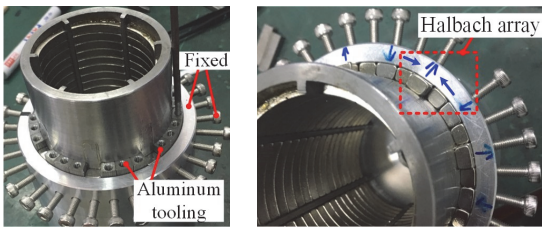

Fig. 23. 16-poles Halbach array manufacturing process. (a) Aluminum tooling. (b) Halbach PM array.

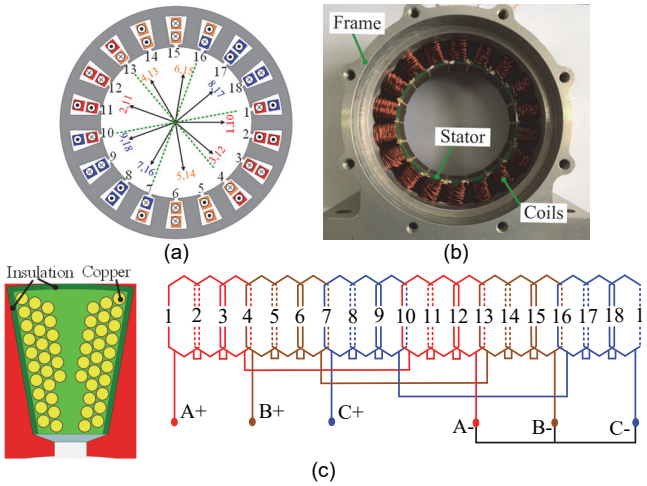

Fig. 24. Cross sections and winding configuration of rotary machine. (a) Stator and winding. (b) Stator prototype. (c) Winding arrangement.

Based on the relationship of the magnetic screw transmission ratio in (2), the rotor rotation at a speed of ω_r =200 r/min, which determines the translator moves at a linear velocity of v_t =0.033 m/s. The rotary speed and torque are coupled with the helical magnetic field to achieve linear motion. The prototype of the magnetic screw can offer 1.5 kN thrust force. Obviously, based on the transmission ratio of maximum thrust force F_t and rotor torque T_n, the value of torque T_n is at least 2.5 Nm.

The no-load back EMF waveform of the rotary machine at speed of 200r/min is shown in Fig. 25(a). The back-EMF is very sinusoidal due to the inherent merit of the FSCW windings and Halbach PM array. Fig. 25(b) shows the harmonic analysis of the back-EMF. It can be seen that the harmonic analysis amplitude to further validate the sinusoidal of the back-EMF. This FSCW PM machine is suitable for brushless AC operation. When using d-axis zero current control and applying nominal current into the three-phase winding, the output torque is shown in Fig. 25(c). It can be seen that torque ripple is insignificant, which benefits from the low cogging torque and sinusoidal back-EMF. Apart from those, the analysis of stator MMF space

This article has been accepted for publication in a future issue of this journal, but has not been fully edited. Content may change prior to final publication. Citation information: DOI 10.1109/TIE.2020.2967731, IEEE Transactions on Industrial Electronics

harmonic is shown in Fig. 25(d). It can be seen that there are abundant harmonics. Therefore, the eddy-current loss of the FSCW PM machine is investigated. The curves of rotor PM eddy-current loss varies from the rotary speed are presented in Fig. 26(a). It can be seen that as the rotational speed increases, the eddy-current loss increases significantly. The steady-state temperature distribution of the rotary machine under rated-load and natural cooling condition is present in Fig. 26(b). Obviously, the temperature is in a reasonable range. The detailed parameters for the PM machine are listed in Table II.

TABLE II
DESIGN SPECIFICATIONS OF PM MACHINE

Item	Value
Outer radius of motor stator, R_{so} (mm)	60
Inner radius of motor rotor, $R_{com\text{-}in}$ (mm)	28.5
Stack length, L_s (mm)	20
Number of slots, S	18
Number of poles, Z	16
Number of phases, N	3
Air-gap length, g_2 (mm)	1
PM thickness, h_{p2} (mm)	5
Angles of radially PM, α_r (deg)	12
Angles of axially PM, α_a (deg)	10.5
Current density, J (A/mm^2)	6.3
Winding factor, k_w	0.945
Magnet remanent, B_{rem} (T)	1.23
Iron lamination	B20AT-1500

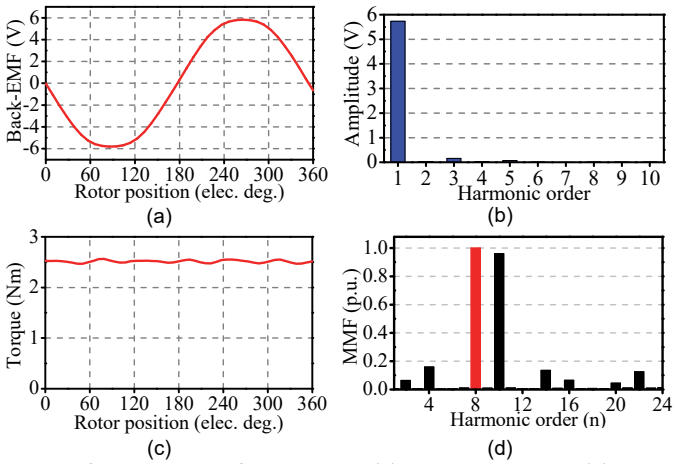

Fig. 25. Characteristics of PM machine. (a) No-load back EMF. (b) EMF harmonic order. (c) Torque. (d) Stator MMF harmonics.

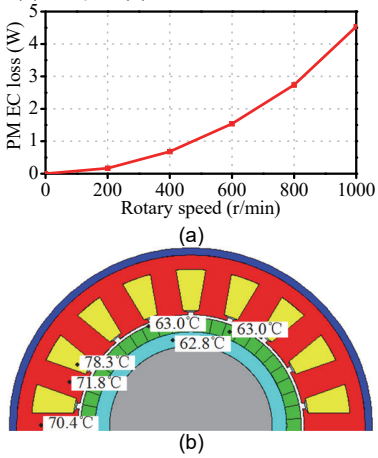

Fig. 26. Losses and temperature distribution. (a) Eddy-current losses. (b) Steady-state temperature under rated-load (200 r/min).

C. Integration Assembly and Mechanical Stress Analysis

The existing integrated designs usually suffer from the eccentricity because of the magnetic attraction and uneven stress point, as shown in Fig. 27. In order to avoid eccentricity and achieve a compact integrated design, an internal plug-in linear bearing solution is used, which has high mechanical strength, low wear, and concentrates the stress point on the axial center of the linear actuator, as shown in Figs. 28(a) and 28(b). The rotary part rotates forward and reverses, and then driving the translator linear reciprocating motion. The ends of the rotary part are fixed by tapered rotary bearings as shown in Fig. 28(c).

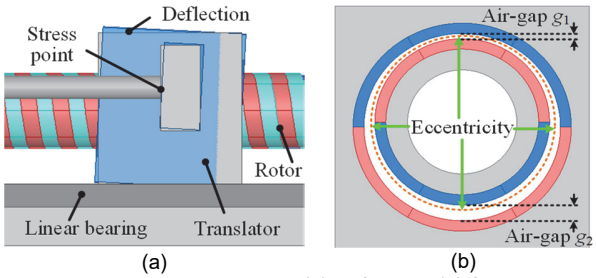

Fig. 27. Existing integrated design. (a) Deflection. (b) Side view.

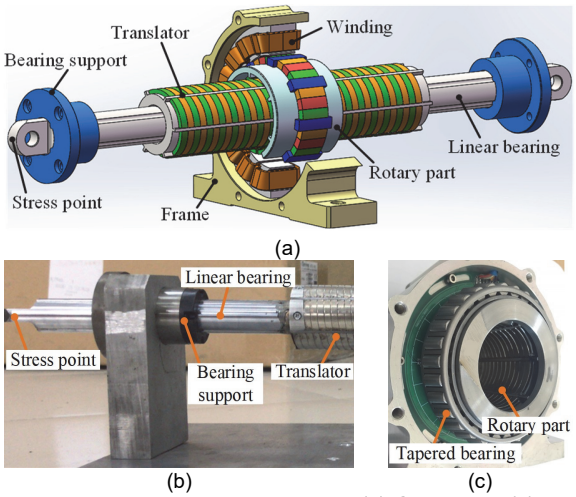

Fig. 28. Proposed integrated assembly. (a) Schematic. (b) Internal plug-in linear bearing. (c) Tapered rotary bearing.

The mechanical stress analysis of the surface-inserted translator without sleeve is shown in Fig. 29(a). It is set that the translator is subjected to a thrust force of 2-kN and reciprocates at a linear speed of 1m/s. Since the discrete PMs are subjected to the axial thrust force and magnetic attraction force, the mechanical stress is mainly distributed on the discrete PMs. It can be seen that the maximum stress is only 3.4MPa, which is much smaller than the tensile strength of the PM materials. Therefore, the topology of the translator is within the safe range of mechanical stress.

In the rotary part, the mechanical stress is much less than the tensile strength of the PM material and iron core material, as shown in Fig. 29(b). Even at 500r/min, the maximum mechanical stress is only 2.01 MPa, and the maximum stress occurs where the discrete PM contacted with the bulge, thereby

This article has been accepted for publication in a future issue of this journal, but has not been fully edited. Content may change prior to final publication. Citation information: DOI 10.1109/TIE.2020.2967731, IEEE Transactions on Industrial Electronics

determining the importance of the bulge. Since the Halbach PM array has the largest radius, the eccentricity force is also the largest. The deformation displacement of the Halbach array is the largest, and the maximum value is about only 0.012 mm, as shown in Fig. 29(c).

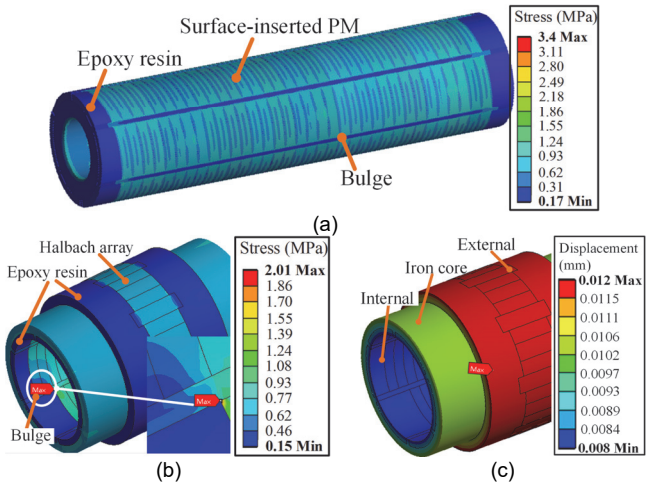

Fig. 29. Mechanical stress and deformation. (a) Translator stress. (b) Rotary part stress. (c) Deformation displacement.

V. Experimental Verification

Fig. 30(a) shows the rotary part of the prototype, while Fig. 30(b) depicts the fully assembled linear electromagnetic actuator mounted on the test bench. The obstacle is installed at the end of the experiment platform, and a force transducer is attached to the end of the translator to obtain the values of thrust force. The linear position encoder is used to measure the translator position and linear speed.

The structure diagram of the control system of this linear electromagnetic actuator based on magnetic screw transmission is shown in Fig. 31. The phase currents are detected by the current sensor, and the circumferentially distributed hall elements are used to achieve the rotary speed and rotor position signals. The linear position sensors can compare the hall signals to determine the relative position between the rotor and the translator.

A. Rotational Characteristic Test

Before assembling the translator, the rotary part is first tested to evaluate the back-EMFs, rotor position hall signals, and torque characteristics. Fig. 32(a) shows the experimental three-phase back-EMFs of the FSCW-PM machine at the rotor speed of 200 r/min, which agrees well with the predicted ones in Fig. 25. The correspondence between hall signals and back-EMFs are presented in Fig. 32(b), which detects the rotor position and rotational speed. Fig. 33 shows the torque and current waveform under d-axis zero current control, in which i_a, i_b, and i_c represent the current waveforms of phases A, B, and C, respectively. The measured values of torque and torque ripple are acceptable, which verifies the effectiveness of the distinct advantages of FSCW-PM machine and Halbach PM array structure.

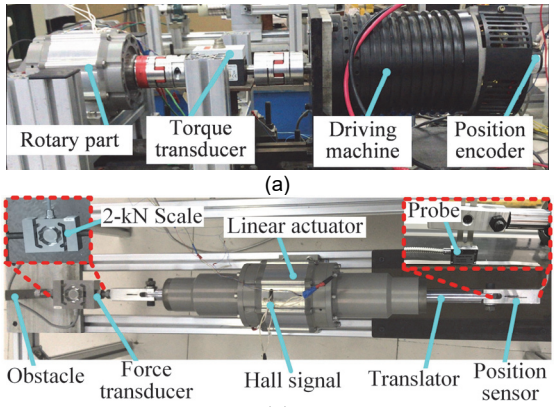

Fig. 30. Experimental platform. (a) Rotary test. (b) Linear test bench.

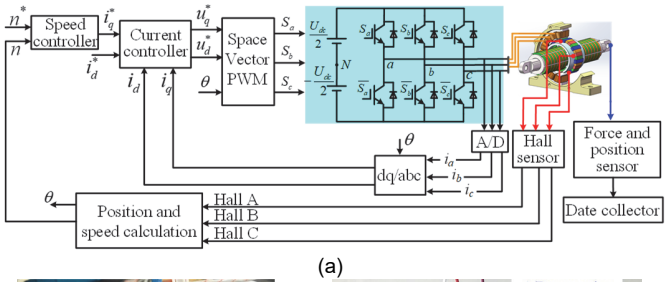

Fig. 31. Control system. (a) Diagram of control. (b) Circular halls. (c) Controller.

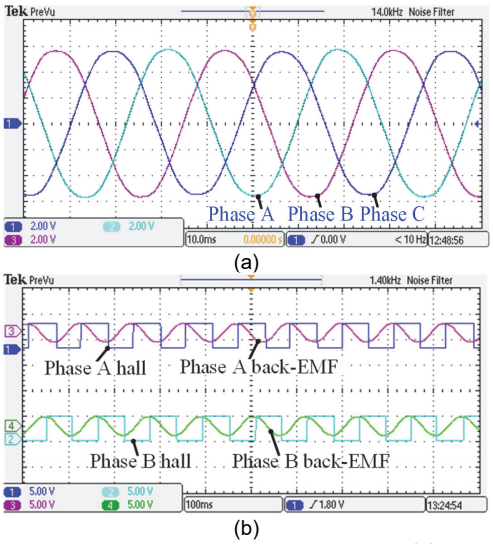

Fig. 32. Measured back-EMFs and hall signals. (a) Back-EMF at 200r/min (2V/div, 10ms/div). (b) Relationship between Hall signals and back-EMFs.

This article has been accepted for publication in a future issue of this journal, but has not been fully edited. Content may change prior to final publication. Citation information: DOI 10.1109/TIE.2020.2967731, IEEE Transactions on Industrial Electronics

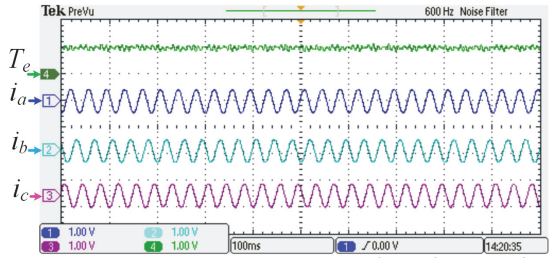

Fig. 33. Measured torque and currents (2N.m/div, 10A/div, and 100ms/div).

B. Thrust Force and Linear Motion Characteristic

Fig. 34(a) depicts the predicted and measured thrust force variations with the different relative position z_d between the rotor and translator. In this 2-poles prototype, the magnetic lead λ is 10mm, at the position of one-quarter of the magnetic lead, the thrust force will reach a maximum value. There is good agreement between the predicted and measured results. The measured thrust force is ~5.2% lower, which is due to the helical effect and end friction. Moreover, the position relationship between the linear displacement and rotary angle is measured, as shown in Fig. 34(b).

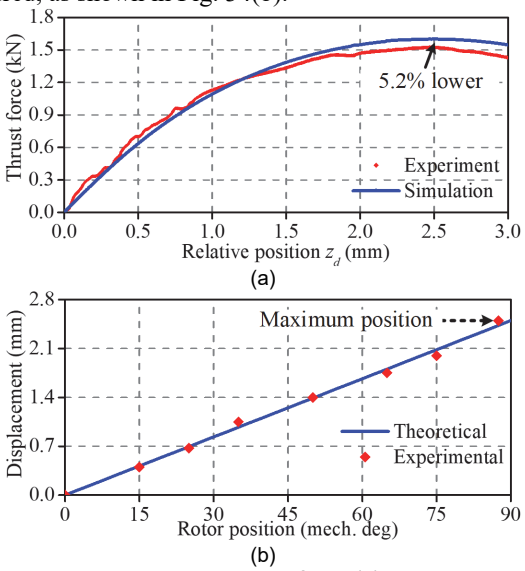

Fig. 34. Predicted and measured thrust force. (a) Variations with relative positon. (b) Linear displacement and angle.

The speed tracking response of both the rotary part and the linear part of the magnetic screw coupling for a 200r/min step rotary speed are tested, as shown in Fig. 35. Based on the operating principle of rotary-linear transmission, the translator should move at a linear speed of 0.033m/s. The rotary speed and position are tested by circular hall elements. It can be seen that the experiment results are tightly around the theoretical results. The linear velocity is tested by a linear position encoder. The linear velocity fluctuates and then tends to stabilize, which is slightly lower than the theoretical value. The errors mainly caused by the position signal accuracy and the end friction. And, the tracking response experiment results also validate the linear speed v_t and rotary angular speed ω_r magnetic screw transmission ratio in (2).

Furthermore, the experiments of the reciprocating motion are shown in Fig. 36. The rotary part rotates forward and reverse directions at 210 r/min, and then driving the translator linearly reciprocating motion almost synchronously. The translator can obtain a linear reciprocating speed of 0.028m/s, and the error is mainly due to the non-contact magnetic transmission and reverse rotation of the rotary part. Also, it can be seen that the experiment of the rotor reciprocating speed is almost asymmetrical. This reason can be attributed to the translator damping and rotor moment of inertia.

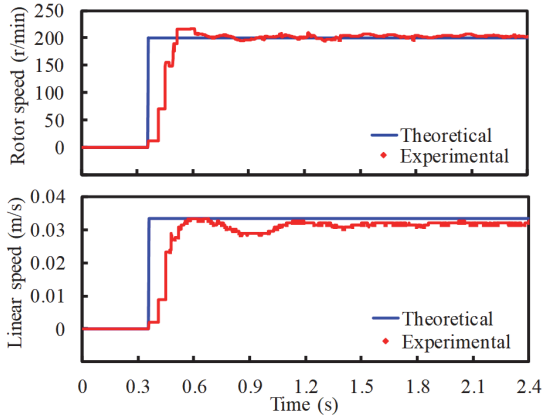

Fig. 35. Predicted and measured speed tracking response.

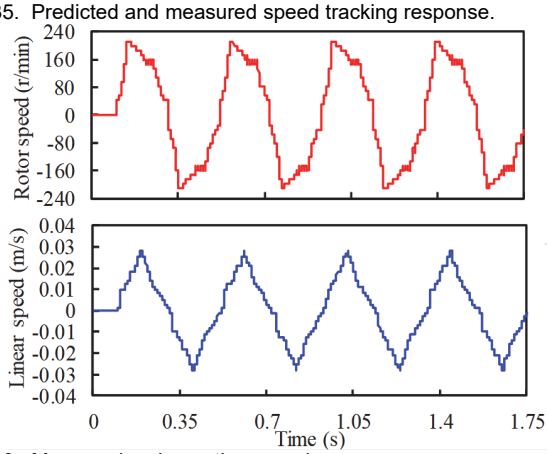

Fig. 36. Measured reciprocating speed response.

VI. Conclusion

In this paper, a linear electromagnetic actuator employing magnetic screw transmission has been described. Key issues for designing and manufacturing the linear actuator has been investigated. Structure simplification and improve accuracy are quite essential in promoting magnetic screw transmission, the surface-inserted approach to employ radial discrete PM to fabricate the helical magnetic pole. Besides, the different number of segmentation has been developed to reduce the cogging effects. The feature of this linear actuator is integrated the rotary machine and magnetic screw overall together and decouples the magnetic circuits. In addition, special bearing supports are used to form a compact integrated design and avoid eccentricity. Finally, a prototype and linear test bench has been constructed, verifying the effectiveness of theoretical analysis and performances.

REFERENCES

[1]. R. Cao, Y. Jin, M. Lu, and Z. Zhang, "Quantitative comparison of linear flux-switching permanent magnet motor with linear induction motor for electromagnetic launch system," *IEEE Trans. Ind. Electron*., vol. 65, no. 9, pp. 7569-7578, Sep. 2018.

[2]. I. Boldea, L. N. Tutelea, W. Xu, and M. Pucci, "Linear electric machines, drives, and MAGLEVs: an overview," *IEEE Trans. Ind. Electron*., vol. 65, no. 9, pp. 7504-7515, Sep. 2018.

[3]. J. Y. Yoon, J. H. Lang, and D. L. Trumper, "Fine-tooth iron-core linear synchronous motor for low acoustic noise application," *IEEE Trans. Ind. Electron*., vol. 65, no. 12, pp. 9895-9904, Dec. 2018.

[4]. C. Zhang and Y. Chen, "Tracking control of ball screw drives using ADRC and equivalent-error-model-based feedforward control," *IEEE Trans. Ind. Electron*., vol. 63, no. 12, pp. 7682-7692, Dec. 2016.

[5]. W. Zhao, J. Zhu, J. Ji, and X. Zhu, "Improvement of power factor in a double side linear flux-modulation permanent-magnet motor for long stroke applications," *IEEE Trans. Ind. Electron*., vol. 66, no. 5, pp. 3391-3400, May 2019.

[6]. Y. Shen, Q. Lu, H. Li, J. Cai, X. Huang, and Y. Fang, "Analysis of a novel double-sided yokeless multitooth linear switched-flux PM motor," *IEEE Trans. Ind. Electron*., vol. 65, no. 2, pp. 1837-1845, Feb. 2018.

[7]. Z. He, F. Dong, J. Zhao, L. Wang, J. Song, Q. Wang, and X. Song, "Thrust ripple reduction in permanent magnet synchronous linear motor based on tuned viscoelastic damper," *IEEE Trans. Ind. Electron*., vol. 66, no. 2, pp. 977-987, Feb. 2019.

[8]. X. Z. Huang, J. Li, Q. Tan, Z. Y. Qian, C. Zhang, and L. Li, "Sectional combinations of the modular tubular permanent magnet linear motor and the optimization design," *IEEE Trans. Ind. Electron*., vol. 65, no. 12, pp. 9658-9667, Dec. 2018.

[9]. M. Cheng, Peng. H, and W. Hua, "General airgap field modulation theory for electrical machines," *IEEE Trans. Ind. Electron*., vol. 64, no. 8, pp. 6063-6074, Aug. 2017.

[10]. M. Johnson, M. C. Gardner, and H. A. Toliyat, "A parameterized linear magnetic equivalent circuit for analysis and design of radial flux magnetic gears—Part I: implementation," *IEEE Trans. Energy Convers*., vol. 33, no. 2, pp. 784-791, Jun. 2018.

[11]. M. Wang, C. Tong, Z. Song, J. Liu, and P. Zheng, "Performance analysis of an axial magnetic-field-modulated brushless double-rotor machine for hybrid electric vehicles," *IEEE Trans. Ind. Electron*., vol. 66, no. 1, pp. 806-817, Jan. 2019.

[12]. J. Wang, K. Atallah, and W. Wang, "Anlysis of a magnetic screw for high force density linear electromagnetic actuators," *IEEE Trans. Magn.*, vol. 47, no. 10, pp. 4477-4480, Oct. 2011.

[13]. R. K. Holm, N. I. Berg , M. Walkusch, P. O. Rasmussen, and R. H. Hansen, "Design of a magnetic lead screw for wave energy conversion," *IEEE Trans. Ind. Appl*., vol. 49, no. 6, pp. 2699-2708, Nov./Dec. 2013.

[14]. K. N. Jenney and S. Pakdelian, "Leakage flux of the trans-rotary magnetic gear," *IEEE Trans. Magn.*, vol. 55, no. 7, Jul. 2019, Art. ID. 8202908.

[15]. F. Gao, Q. Wang, Y. Hu, B. Chen, B. Zhao, and J. Zou, "Performance evaluation of magnetic lead screws equipped with skewed arc magnet instead of helical ones," *IEEE Trans. Magn.*, vol. 54, no. 11, Nov. 2018, Art. ID. 8204405.

[16]. C. S. Cyusa and Y. Fujimoto, "Enactment-based direct-drive test of a novel radial-gap helical RotLin machine," *IEEE Trans. Ind. Appl*., vol. 54, no. 2, pp. 1273-1282, Mar./Apr. 2018.

[17]. A. Abolhasani and S. Pakdelian, "Equivalent circuit for the trans-rotary magnetic gear," *IEEE Trans. Ind. Electron*., vol. 66, no. 10, pp. 8266-8272, Oct. 2019.

[18]. M. B. Kouhshahi, J. Kadel, J. Bird, and W. Williams, "Designing and experimentally testing a magnetically geared lead screw," *IEEE Trans. Ind. Appl*., vol. 54, no. 6, pp. 5736-5747, Nov./Dec. 2018.

[19]. M. Cirolini, A. F. Filho, Y. C. Wu, and D. G. Dorrell, "Design aspect of a reluctance-based magnetic lead screw," *IEEE Trans. Magn.*, vol. 55, no. 7, Jul. 2019, Art. ID. 8001906.

[20]. A. Heya, Y. Nakata, M. Sakai, H. Ishiguro, and K. Hirata, "Force estimation method for a magnetic lead-screw-driven linear actuator," *IEEE Trans. Magn.*, vol. 54, no. 11, Nov. 2018, Art. ID. 8207805.

[21]. S. Pakdelian, N. W. Frank, and H. A. Toliyat, "Magnetic design aspects of the trans-rotary magnetic gear," *IEEE Trans. Energy Convers*., vol. 30, no. 1, pp. 41-50, Mar. 2015.

[22]. Z. Ling, J. Ji, J. Wang, and W. Zhao, "Design optimization and test of a radially magnetized magnetic screw with discretized PMs," *IEEE Trans. Ind. Electron*., vol. 65, no. 9, pp. 7536-7547, Sep. 2018.

[23]. K. Lu, Y. Xia, W. Wu and L. Zhang, "New helical-shape magnetic pole design for magnetic lead screw enabling structure simplification," *IEEE Trans. Magn*., vol. 51, no. 11, Nov. 2015, Art. ID. 8204404.

[24]. N. Vitale, "Rotary torque to axial force energy conversion apparatus," Nov. 16 1999, US Patent 5,984,960.

[25]. S. Pakdelian, Y. B. Deshpande, and H. A. Toliyat, "An electric machine integrated with trans-rotary magnetic gear," *IEEE Energy Conversion Congress and Exposition* (*ECCE*), pp. 3356-3362, Sep. 2012.

[26]. S. Pakdelian, Y. B. Deshpande, and H. A. Toliyat, "Design of an electric machine integrated with trans-rotary magnetic gear," *IEEE Trans. Energy Convers*., vol. 30, no. 3, pp. 1180-1191, Sep. 2015.

[27]. N. I. Berg, A. B. Christiansen, R. K. Holm, and P. O. Rasmussen, "Design and test of a reluctance based magnetic lead screw PTO system for a wave energy converter," *IEEE International Electric Machines and Drives Conference*, May 2017.

[28]. N. I. Berg, R. K. Holm, and P. O. Rasmussen, "Design and development of a MLS based compact active suspension system, featuring air spring and energy harvesting capabilities," *IEEE Energy Conversion Congress and Exposition*, Feb. 2017.

Zhijian Ling (S'16) received the B. Sc degree degree in electrical engineering and automation from Shandong Agriculture University, Taian, China, in 2013, and the M.Sc degree in electrical engineering from Jiangsu University, Zhenjiang, China, in 2016. where he is currently working toward the Ph.D degree. From September 2018 to August 2019, he was a joint Ph.D. student funded in the Department of Energy Technology, Aalborg University, Aalborg, Denmark.

His research interests include the design and analysis of permanent magnet electrical machines, and magnetic actuators.

Wenxiang Zhao (M'08-SM'14) received the B.Sc. and M.Sc. degrees from Jiangsu University, Zhenjiang, China, in 1999 and 2003, respectively, and the Ph.D. degree from Southeast University, Nanjing, China, in 2010, all in electrical engineering. He has been with Jiangsu University since 2003, where he is currently a Professor with the School of Electrical Information Engineering.

From 2008 to 2009, he was a Research Assistant with the Department of Electrical and Electronic Engineering, University of Hong Kong, Hong Kong. From 2013 to 2014, he was a Visiting Professor with the Department of Electronic and Electrical Engineering, University of Sheffield, Sheffield, U.K. His current research interests include electric machine design, modeling, fault analysis, and intelligent control. He has authored and co-authored over 250 technical papers in these areas.

Peter Omand Rasmussen (M'98) was born in Aarhus, Denmark, in 1971. He received the M.Sc. and Ph.D. degrees from Aalborg University, Aalborg, Denmark, in 1995 and 2001, respectively, all in electrical engineering.

In 1998, he became an Assistant Professor, and in 2002, he became an Associate Professor with Aalborg University. His research interests include the design and control of switched reluctance, permanent magnet machines, and magnetic gears.

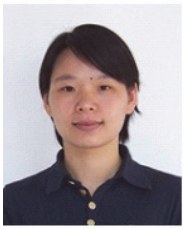

Jinghua Ji received the B.Sc., M.Sc., and Ph.D. degrees in electrical engineering from Jiangsu University, Zhenjiang, China, in 2000, 2003, and 2009, respectively.

Since 2000, she has been with the School of Electrical and Information Engineering, Jiangsu University, where she is currently a Professor. From 2013 to 2014, she was a Visiting Scholar with the Department of Electronic and Electrical Engineering, University of Sheffield, Sheffield, U. K. Her areas of interest include motor design and electromagnetic field computation. She has authored and co-authored over 100 technical papers in these areas.

Yang Jiang received the B.Sc. degree in electrical engineering from Tongda College of Nanjing University of Posts and Telecommunications, Yangzhou, China, in 2017, and he is currently working toward the M.Sc. degree in electrical engineering from Jiangsu University, Zhenjiang, China.

His research interests include control of permanent-magnet machines.

Zhengmeng Liu received the B.Sc. degree in electrical engineering from Chongqing University, Chongqing, China, in 2013. and the M.Sc. degree in electrical engineering from Jiangsu University, Zhenjiang, China, in 2016. He is currently pursuing the Ph.D. degree with University of Sheffield, Sheffield, U.K.,

His current research interests include linear actuator design.